Report no. 01/19

A spectral Petrov-Galerkin formulation for pipe flow II: Nonlinear transitional stages

A. Meseguer
L. N. Trefethen

Oxford University Computing Laboratory
Numerical Analysis Group
Wolfson Building
Parks Road
Oxford, England OX1 3QD

October, 2001

Abstract

This work is devoted to the study of the nonlinear evolution of perturbations of Hagen-Poiseuille or pipe flow. We make use of a solenoidal spectral Petrov-Galerkin method for the spatial discretization of the Navier-Stokes equations for the perturbation field. For the time evolution, we use a semi-implicit time integration scheme. Special attention is given to the explicit treatment and efficient evaluation of the nonlinear terms. The hydrodynamic stability analysis is focused on the *streak breakdown* process by which two-dimensional streamwise-independent perturbations transiently modulate the basic flow, resulting in a profile which is linearly unstable with respect to three-dimensional perturbations. This mechanism is one possible route of transition to turbulence in subcritical shear flows.

1 Introduction

Hydrodynamic instability of pipe flow remains one of the unsolved problems of fundamental fluid dynamics. Pipe or plane Couette problems belong to a particular familiy of shear flows which are usually termed *subcritical*. From a mathematical point of view, these flows are linearly stable, i.e., the spectrum of the linearized Navier-Stokes operator around the basic flow always lies on the stable half of the complex plane. Therefore, any infinitesimal perturbation added to the basic flow must eventually decay. Nevertheless, these flows become turbulent in the laboratory. Pipe flow, for example, becomes turbulent in experiments for Re ~ 2200 or higher (Darbyshire & Mullin, 1995). Experimental and numerical evidence suggest that transition in pipe flow is extremely sensitive to the size and structure of the perturbations. Pipe flow instability differs from that of other classical flows such as Taylor-Couette or Rayleigh-Benard where the basic profile becomes unstable by means of a local bifurcation (Drazin & Reid, 1981). In those problems, the instability is characterized by a sharp critical value of the control parameter, the Reynolds number or the Rayleigh number, above which the basic flow becomes linearly unstable. In that case, the agreement between experimental results and numerical simulations is very good. Besides, in these problems, the flow is confined to a finite size domain, i.e., they are *enclosed* flows. Pipe flow is a prototype of *open* flow and its study is more complicated. In open flows, the perturbations are eventually advected downstream and they leave the domain, making it impossible sometimes to determine the laminar-turbulent character of the dynamics for long times. Another difficulty arises when the open flows are modelled numerically by artificially assuming periodicity in the streamwise direction of the flow.

The numerical simulation of pipe flows is not a new matter. This problem has been previously simulated by different numerical schemes in the recent past. Among other works, we should mention (Boberg & Brosa, 1988), (Leonard & Reynolds, 1988), (O'Sullivan & Breuer, 1994), (Priymak & Miyazaki, 1998), (Shan *et al.*, 1999) and (Komminaho, 2000). In (Meseguer & Trefethen, 2000), the linear stability and transient growth of perturbations in pipe flow were studied by means of the linearization of the Navier-Stokes equations. In that work, it was found that streamwise-independent vortices were optimally amplified by linear nonnormal mechanisms. It has long been known that streamwise vortices are crucial in the transition to turbulence of subcritical shear flows (Schmid & Henningson, 2001). These two-dimensional structures grow transiently and modulate the basic flow, leading to a new velocity profile which contains *streaks*, i.e., regions where the flow attains high or low relative speeds. This new flow contains saddle points and, in a transient sense, is linearly unstable with respect to three-dimensional perturbations (Reddy *et al.*, 1998). We refer the reader to the recent monograph

(Schmid & Henningson, 2001) on stability of shear flows for details.

The main goal of this work is to study the nonlinear time evolution of perturbations in pipe flow. We focus our attention on the initial stages of transition to turbulence; the study of fully developed turbulent flow is beyond our scope. For this purpose, we use the spectral method formulated in (Meseguer & Trefethen, 2000) for the spatial discretization of the linear Navier-Stokes operator and we formulate a pseudospectral (collocation) method for the computation of the nonlinear terms. For the time integration, we use a semi-implicit (or linearly implicit) scheme.

The study is structured as follows. In §2, the problem is formulated physically. In this section we obtain the nonlinear partial differential equations which dictate the evolution of the perturbations. In §3 we provide a brief summary of the spectral method used to discretize the linear part of the equations. In §4, the time marching method is explained in detail and special emphasis is given to the explicit evaluation of the nonlinear terms. Section §5 is a standard convergence test, where the accuracy and computational cost of different time marching schemes are compared. A comparison with previous numerical computations of streamwise perturbations is provided in section §6. Finally, in §7, we focus our attention on the streak breakdown route to transition.

2 The nonlinear initial value problem

We consider the motion of an incompressible viscous fluid of kinematic viscosity ν and density ρ. The fluid is driven through a circular pipe of radius a and infinite length by a uniform pressure gradient, Π_0, parallel to the axis of the pipe. The motion of the fluid is governed by the incompressible Navier-Stokes equations

$$\partial_t \mathbf{v} + (\mathbf{v}\cdot\nabla)\mathbf{v} = -\frac{\Pi_0}{\rho}\hat{\boldsymbol{z}} - \nabla p + \nu\Delta\mathbf{v} \tag{2.1}$$

$$\nabla\cdot\mathbf{v} = 0, \tag{2.2}$$

where $\mathbf{v}$ is the velocity vector field, satisfying the no-slip boundary condition at the wall,

$$\mathbf{v}_{\text{pipe wall}} = \mathbf{0}, \tag{2.3}$$

and p is the reduced pressure. We formulate the problem in cylindrical coordinates. The velocity of the fluid is prescribed by its radial ($\hat{\boldsymbol{r}}$), azimuthal ($\hat{\boldsymbol{\theta}}$) and axial ($\hat{\boldsymbol{z}}$) components

$$\mathbf{v} = u\,\hat{\boldsymbol{r}} + v\,\hat{\boldsymbol{\theta}} + w\,\hat{\boldsymbol{z}} = (u\ ,\ v\ ,\ w), \tag{2.4}$$

where u, v and w depend on the three spatial coordinates (r,θ,z) and time t. A basic steady solution of (2.1), (2.2) and (2.3) is the so-called *Hagen-Poiseuille flow*

$$\mathbf{v}_{\mathrm{B}} = (u_{\mathrm{B}}\ ,\ v_{\mathrm{B}}\ ,\ w_{\mathrm{B}}) = \left(0\ ,\ 0\ ,\ -\frac{\Pi_0 a^2}{4\rho\nu}\left[1-\left(\frac{r}{a}\right)^2\right]\right), \quad p_{\mathrm{B}} = \Pi_0 z + \mathrm{C}, \tag{2.5}$$

where C is an arbitrary constant. This basic flow is a parabolic axial velocity profile which only depends on the radial coordinate (Batchelor, 1967). The velocity of the fluid attains a maximum value $U_{\mathrm{CL}} = -\Pi_0 a^2/4\rho\nu$ at the center-line or axis of the cylinder.

Henceforth, all variables will be rendered dimensionless using a and U_{CL} as space and velocity units, respectively. The axial coordinate z is unbounded since the length of the pipe

is infinite. In what follows, we assume that the flow is axially periodic with period b. This assumption, though physically artificial, enables us to study many phenomena for an infinite pipe provided b is not too small. In the dimensionless system, the spatial domain Ω of the problem is

$$\Omega = \{\ (r,\theta,z) \mid 0 \le r \le 1,\ \ 0 \le \theta < 2\pi,\ \ 0 \le z < Q\} \tag{2.6}$$

where $Q = b/a$. In the new variables, the basic flow takes the form

$$\mathbf{v}_{\mathrm{B}} = (u_{\mathrm{B}}, v_{\mathrm{B}}, w_{\mathrm{B}}) = (0\ ,\ 0\ ,\ 1 - r^2). \tag{2.7}$$

Finally, the parameter which governs the dynamics of the problem is the *Reynolds number*

$$\mathrm{Re} = \frac{aU_{\mathrm{CL}}}{\nu}. \tag{2.8}$$

For the stability analysis, we suppose that the basic flow is perturbed by a solenoidal velocity field vanishing at the pipe wall

$$\mathbf{v}(r,\theta,z,t) = \mathbf{v}_{\mathrm{B}}(r) + \mathbf{u}(r,\theta,z,t), \quad \nabla\cdot\mathbf{u} = 0, \quad \mathbf{u}(r=1) = \mathbf{0}, \tag{2.9}$$

and a perturbation pressure field

$$p(r,\theta,z,t) = p_{\mathrm{B}}(z) + q(r,\theta,z,t). \tag{2.10}$$

On introducing the perturbed fields in the Navier-Stokes equations, we obtain a nonlinear initial-boundary problem for the perturbations $\mathbf{u}$ and q:

$$\begin{aligned}
\partial_t\mathbf{u} &= -\nabla q + \frac{1}{\mathrm{Re}}\Delta\mathbf{u} - (\mathbf{v}_{\mathrm{B}}\cdot\nabla)\mathbf{u} - (\mathbf{u}\cdot\nabla)\mathbf{v}_{\mathrm{B}} - (\mathbf{u}\cdot\nabla)\mathbf{u}, && (2.11)\\
\nabla\cdot\mathbf{u} &= 0, && (2.12)\\
\mathbf{u}(1,\theta,z,t) &= 0, && (2.13)\\
\mathbf{u}(r,\theta+2\pi n,z,t) &= \mathbf{u}(r,\theta,z,t), && (2.14)\\
\mathbf{u}(r,\theta,z+lQ,t) &= \mathbf{u}(r,\theta,z,t), && (2.15)\\
\mathbf{u}(r,\theta,z,0) &= \mathbf{u}_0, \quad \nabla\cdot\mathbf{u}_0 = 0, && (2.16)
\end{aligned}$$

for $(n,l) \in \mathbb{Z}^2$, $(r,\theta,z) \in [0,1]\times[0,2\pi)\times[0,Q)$ and $t > 0$. Equation (2.11) describes the nonlinear space-time evolution of the perturbation of the velocity field. Equation (2.12) is the solenoidal condition for the perturbation, and equations (2.13)–(2.15) describe the homogeneous boundary condition for the radial coordinate and the periodic boundary conditions for the azimuthal and axial coordinates respectively. Finally, equation (2.16) is the initial solenoidal condition for the perturbation field at $t = 0$.

For the linear stability analysis, carried out in (Meseguer & Trefethen, 2000), we neglected the convective nonlinear term $(\mathbf{u}\cdot\nabla)\mathbf{u}$. The linearity of the operator arising in the stability analysis allowed us to decouple the various axial and azimuthal modes. As a result, the problem was greatly simplified because its integration in space and time was reduced to the independent computation of the evolution of each periodic axial-azimuthal mode. This procedure involved the integration of *one*-dimensional initial-boundary problems involving the radial variable only. In the present case, the term $(\mathbf{u}\cdot\nabla)\mathbf{u}$ in (2.11) will couple different axial and azimuthal modes by means of certain selection rules.

3 Spectral Petrov-Galerkin scheme: summary

Following (Meseguer & Trefethen, 2000), henceforth referred to as M&T, we discretize the perturbation field $\mathbf{u}$ in (2.11)-(2.16) by a spectral approximation $\mathbf{u}_{\mathrm{S}}$ of order L in z, order N in θ, and order M in r,

$$\mathbf{u}_{\mathrm{S}}(r,\theta,z,t) = \sum_{l=-L}^{L}\sum_{n=-N}^{N}\sum_{m=0}^{M} a_{lnm}(t)\mathbf{\Phi}_{lnm}(r,\theta,z), \tag{3.1}$$

where $\mathbf{\Phi}_{lnm}$ are *trial* bases of solenoidal vector fields of the form

$$\mathbf{\Phi}_{lnm}(r,\theta,z) = \mathrm{e}^{\mathrm{i}(2\pi lz/Q+n\theta)}\mathbf{v}_{lnm}(r), \tag{3.2}$$

satisfying

$$\nabla\cdot\mathbf{\Phi}_{lnm} = 0 \tag{3.3}$$

for $l=-L,\dots,L$, $n=-N,\dots,N$ and $m=0,\dots,M$. The trial bases (3.2) are analytic, periodic in the axial and azimuthal directions, and satisfy homogeneous boundary conditions,

$$\mathbf{\Phi}_{lnm}(1,\theta,z) = \mathbf{0}, \tag{3.4}$$

at the wall. Therefore, equations (2.12)–(2.15) are identically satisfied by our spectral approximation. The spectral Petrov-Galerkin scheme is accomplished by substituting expansion (3.1) in (2.11) and projecting over a set of *test* vector fields

$$\mathbf{\Psi}_{lnm}(r,\theta,z) = \mathrm{e}^{\mathrm{i}(2\pi lz/Q+n\theta)}\tilde{\mathbf{v}}_{lnm}(r), \tag{3.5}$$

satisfying

$$\nabla\cdot\mathbf{\Psi}^{(1,2)}_{lnm} = 0. \tag{3.6}$$

Explicit expressions for the trial and test fields, $\mathbf{v}_{lnm}$, $\tilde{\mathbf{v}}_{lnm}$, can be found in Appendix A. Overall, the projection scheme is summarized by

$$(\mathbf{\Psi}_{lnm}\ ,\ \partial_t\mathbf{u}_{\mathrm{S}}) = \left(\mathbf{\Psi}_{lnm}\ ,\ \frac{1}{\mathrm{Re}}\Delta\mathbf{u}_{\mathrm{S}} - (\mathbf{v}_{\mathrm{B}}\cdot\nabla)\mathbf{u}_{\mathrm{S}} - (\mathbf{u}_{\mathrm{S}}\cdot\nabla)\mathbf{v}_{\mathrm{B}} - (\mathbf{u}_{\mathrm{S}}\cdot\nabla)\mathbf{u}_{\mathrm{S}}\right), \tag{3.7}$$

for $l=-L,\dots,L$, $n=-N,\dots,N$ and $m=0,\dots,M$, where the inner product $(\cdot,\cdot)$ is the volume integral over the domain of the pipe:

$$(\mathbf{a},\mathbf{b}) = \int_0^Q\int_0^{2\pi}\int_0^1 \mathbf{a}^*\cdot\mathbf{b}\ r\mathrm{d}r\ \mathrm{d}\theta\ \mathrm{d}z. \tag{3.8}$$

We have not included the pressure term ∇q of (2.11) in the projection scheme (3.7). One of the advantages of our method is that the pressure term is cancelled in the projection, i.e.,

$$(\mathbf{\Psi}_{lnm}\ ,\ \nabla q) = 0; \tag{3.9}$$

see (Canuto *et al.*, 1988) or (Leonard & Wray, 1982), for example.

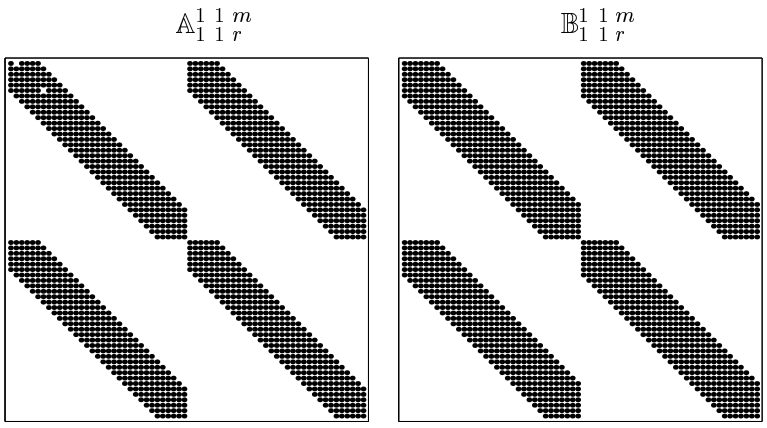

Figure 1: Sparse structure of operators $\mathbb{A}^{lnm}_{pqr}$ and $\mathbb{B}^{lnm}_{pqr}$ for $l = p = 1$ and $n = q = 1$, with $M = 32$ radial modes

Once the projection has been carried out, the spatial dependence has been eliminated from the problem and a nonlinear dynamical system for the amplitudes a_{lnm} is obtained. Symbolically, this system reads

$$\mathbb{A}^{lnm}_{pqr}\ \dot{a}_{pqr} = \mathbb{B}^{lnm}_{pqr}\ a_{pqr} - b_{lnm}(a, a), \tag{3.10}$$

where we have used the convention of summation with respect to repeated indices. The discretized operator $\mathbb{A}$ appearing in (3.10) is the projection

$$\mathbb{A}^{lnm}_{pqr} = (\mathbf{\Psi}_{lnm}\ ,\ \mathbf{\Phi}_{pqr}) = 2\pi Q \delta^l_p \delta^n_q \int_0^1 \tilde{\mathbf{v}}^*_{lnm} \cdot \mathbf{v}_{pqr} r \mathrm{d}r, \tag{3.11}$$

where δ^i_j is the Kronecker symbol. The inner product (3.11) reveals another advantage of the Galerkin scheme. First, due to the linearity of the time diferentiation operator ∂_t and the Fourier orthogonality in the periodic variables, the axial and azimuthal modes decouple. The operator $\mathbb{B}$ in (3.10),

$$\mathbb{B}^{lnm}_{pqr} = \left(\mathbf{\Psi}_{lnm}\ ,\ \frac{1}{\mathrm{Re}}\Delta\mathbf{\Phi}_{pqr} - (\mathbf{v}_\mathrm{B}\cdot\nabla)\mathbf{\Phi}_{pqr} - (\mathbf{\Phi}_{pqr}\cdot\nabla)\mathbf{v}_\mathrm{B}\right), \tag{3.12}$$

satisfies the same orthogonality properties in the periodic variables. Second, the functions $\tilde{\mathbf{v}}_{lnm}(r)$ and $\mathbf{v}_{pqr}(r)$ are made of shifted Chebyshev polynomials in the radial variable. As a result, those operators $\mathbb{A}^{lnm}_{pqr}$ and $\mathbb{B}^{lnm}_{pqr}$ with different axial indices ($l \neq p$) or different azimuthal ones ($n \neq q$) are identically zero. The remaining operators with $l = p$ and $n = q$ have a banded structure due to the pseudo-orthogonality properties of the shifted Chebyshev basis used in the radial variable. In figure 1 we have represented the sparse structure of both operators for the particular case $l = p = 1$, $n = q = 1$.

The quadratic form $b_{lnm}(a, a)$ appearing in (3.10) corresponds to the projection of the nonlinear convective term

$$(\mathbf{\Psi}_{lnm}\ ,\ (\mathbf{u}_\mathrm{S}\cdot\nabla)\mathbf{u}_\mathrm{S})\,. \tag{3.13}$$

For computational efficiency, this term has to be calculated via a pseudospectral method. The details of this computation will be analyzed in the next section. Finally, the initial value problem is prescribed by the coefficients $a_{lnm}(0)$ representing the initial vector field $\mathbf{u}_{\mathrm{S}}^0$ given by

$$a_{lnm}(t=0) = \left(\mathbf{\Psi}_{lnm}\ ,\ \mathbf{u}_{\mathrm{S}}^0\right). \tag{3.14}$$

The next section will deal with the integration in time of the initial value problem (3.10)-(3.14).

In our spectral analysis, we used complex Fourier expansions in the axial and azimuthal variables. The main motivation for this was simplicity in the orthogonality properties of the inner products in the projection scheme. In order to avoid redundant computations, we still can take advantage of the fact that our vector approximation (3.1) is a real object, i.e.,

$$\mathbf{u}_{\mathrm{S}}^* = \mathbf{u}_{\mathrm{S}}, \tag{3.15}$$

where * stands for complex conjugate. From (3.1), condition (3.15) implies that

$$a_{-l,\,-n,\ m}\ \mathbf{\Phi}_{-l,\,-n,\ m} = a_{lnm}^*\ \mathbf{\Phi}_{lnm}^*, \quad \forall m. \tag{3.16}$$

Since the elements of our trial basis (3.2) satisfy

$$\mathbf{\Phi}_{-l,\,-n,\ m} = \mathbf{\Phi}_{lnm}^*, \quad \forall m, \tag{3.17}$$

the conjugation rule (3.17) implies that

$$a_{-l,\,-n,\ m} = a_{lnm}^*, \quad \forall m, \tag{3.18}$$

which considerably reduces the number of independent degrees of freedom, the computational cost and storage.

4 Time marching and efficient computation of $(\mathbf{u}_{\mathrm{S}} \cdot \nabla)\mathbf{u}_{\mathrm{S}}$

4.1 Overview

The spectral spatial discretization of the Navier-Stokes equations leads to a system of ODEs which is *stiff* (Iserles, 1996). A stiff system is characterized by the presence of modes with vastly different time-scales. This pathology leads to stability problems in the time discretization. Explicit time integration schemes fail in the presence of stiffness (Hairer & Wanner, 1991). The development of numerical algorithms for the solution of stiff systems is an active research area where new methodologies appear frequently. In spectral discretization of nonlinear PDEs, the more standard procedures are based on *semi-implicit*, also called *linearly implicit* methods, where the linear part is integrated implicitly and the nonlinear terms are treated explicitly (Boyd, 1999).

To overcome stiffness in our particular problem, different methods such as *Strang Splitting* (**SS**) or *Exponential Time Differencing* (**ETD**), have been applied, see (Yosida, 1990) or (Cox & Matthews, 2001). Among the different methodologies used, we found implicit backwards differences combined with explicit *Adams-Bashforth* schemes the most suitable for our problem. We proceed to formulate the scheme that has been used for most of the computations carried out in this work.

4.2 Linearly implicit time integration

Let Δt be the time step and $t^{(k)} = k\,\Delta t, \quad k = 0, 1, 2, \ldots$ the time array where we approximate our amplitudes $a(t)$ [1] from the original system (3.10). In our notation, $a^{(k)} = a(t^{(k)})$ is the approximation of $a(t)$ at $t = t^{(k)}$ and $b^{(k)}$ is the nonlinear quadratic form appearing in (3.10) evaluated at $t^{(k)}$, i.e., $b^{(k)} = b(a^{(k)}, a^{(k)})$. The fourth-order *Backwards Differentiation/Adams-Bashforth* method, henceforth referred as **BD4AB4** (Cox & Matthews, 2001), is

$$\begin{array}{rcl} (25\ \mathbb{A} - 12\ \Delta t\ \mathbb{B})\ a^{(k+1)} & = & \mathbb{A}\left(48a^{(k)} - 36a^{(k-1)} + 16a^{(k-2)} - 3a^{(k-3)}\right) \\ & & -\Delta t\ \left(48b^{(k)} - 72b^{(k-1)} + 48b^{(k-2)} - 12b^{(k-3)}\right) \end{array} , \tag{4.1}$$

for $k = 3, 4, 5, \ldots$. The initial value $a^{(0)}$ is prescribed by the initial condition and the first three amplitudes $a^{(1,2,3)}$ are obtained by a fourth-order *Runge-Kutta* explicit method, henceforth referred as **RK4** (Hairer & Wanner, 1991), given by

$$a^{(k+1)} = a^{(k)} + \frac{1}{6}\left(\alpha + 2\beta + 2\gamma + \phi\right), \tag{4.2}$$

where

$$\begin{array}{rcl} \mathbb{A}\,\alpha & = & \Delta t\,\mathbb{B}\,a^{(k)} - \Delta t\,b\left(a^{(k)}, a^{(k)}\right) \\ \mathbb{A}\,\beta & = & \Delta t\,\mathbb{B}\left(a^{(k)} + \alpha/2\right) - \Delta t\,b\left(a^{(k)} + \alpha/2, a^{(k)} + \alpha/2\right) \\ \mathbb{A}\,\gamma & = & \Delta t\,\mathbb{B}\left(a^{(k)} + \beta/2\right) - \Delta t\,b\left(a^{(k)} + \beta/2, a^{(k)} + \beta/2\right) \\ \mathbb{A}\,\phi & = & \Delta t\,\mathbb{B}\left(a^{(k)} + \gamma\right) - \Delta t\,b\left(a^{(k)} + \gamma, a^{(k)} + \gamma\right), \end{array} \tag{4.3}$$

for $k = 0, 1, 2$. From equations (4.1) and (4.3), we see that we need to evaluate explicitly the nonlinear term at different previous stages, i.e., to evaluate $b(a, a)$ in (4.1) for the pre-computed amplitudes $a^{(k)}$, $a^{(k-1)}$, $a^{(k-2)}$ and $a^{(k-3)}$, and in (4.3) for $a^{(k)}$, $a^{(k)} + \alpha/2$, $a^{(k)} + \beta/2$ and $a^{(k)} + \gamma$. The next section is devoted to the efficient computation of b by means of a *de-aliased* pseudospectral or collocation method.

4.3 Evaluation of nonlinear terms: pseudospectral method

In this section, we study how to evaluate the non-linear term

$$b_{lnm} = (\mathbf{\Psi}_{lnm}, (\mathbf{u}_S \cdot \nabla)\mathbf{u}_S) = \int_0^Q \int_0^{2\pi} \int_0^1 \mathbf{\Psi}^*_{lnm} \cdot (\mathbf{u}_S \cdot \nabla)\mathbf{u}_S \; r\mathrm{d}r\; \mathrm{d}\theta\; \mathrm{d}z, \tag{4.4}$$

where $\mathbf{u}_S$ is given by the expansion (3.1). This term plays a very important role in the time integration scheme since a high percentage of the computational time is used here. Many references on spectral Galerkin methods tacitly mention the pseudospectral technique for the efficient computation of nonlinear terms. A detailed analysis of this procedure can be found in (Boyd, 1999) in a general framework. The standard procedure for the computation of the nonlinear advective term is summarized in the diagram of figure 2. Basically, once the coefficients a_{lnm} (top left of the diagram) of $\mathbf{u}_S$ are known, we evaluate $\mathbf{u}_S$ in the physical space (top arrow going from left to right in the diagram). The gradient of the vector field, $\nabla\mathbf{u}_S$, and the convective product, $(\mathbf{u}_S \cdot \nabla)\mathbf{u}_S$, are also computed in the physical space (vertical arrows downwards, on the right). Finally, the physical product is projected onto the dual Fourier-Chebyshev space (bottom arrow, from right to left). We proceed to explain in detail each one of the three computational stages.

[1] To avoid cumbersome notation, we temporarily suppress the indices corresponding to the spectral discretization.

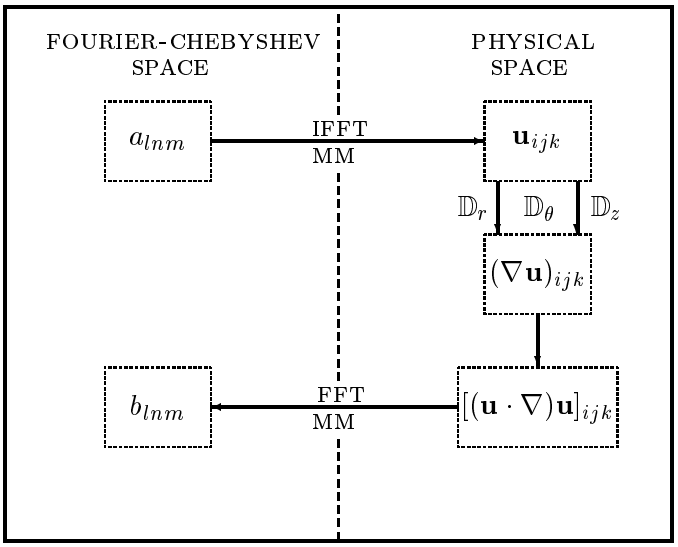

Figure 2: Pseudospectral computation of nonlinear terms. The abbreviations FFT, IFFT and MM stand for *Fast Fourier Transform*, *Inverse Fast Fourier Transform* and *Matrix Multiplication*, respectively.

(I) EVALUATION OF $\mathbf{u}_{\rm S}$ IN PHYSICAL SPACE

The first stage of the algorithm is to evaluate the sum (3.1)

$$\mathbf{u}_{\rm S} = \sum_{l=-L}^{L}\sum_{n=-N}^{N}\sum_{m=0}^{M} a_{lnm}(t)\mathbf{\Phi}_{lnm}(r,\theta,z) = \sum_{l=-L}^{L}\sum_{n=-N}^{N}\sum_{m=0}^{M} a_{lnm}\, \mathrm{e}^{\mathrm{i}(n\theta+2\pi lz/Q)}\mathbf{v}_{lnm}(r) \qquad (4.5)$$

over the three-dimensional grid

$$(r_k,\theta_j,z_i) = \left(\cos(\frac{\pi k}{2M_d})\,,\ \frac{2\pi}{N_d}j\,,\ \frac{Q}{L_d}i\right), \qquad (4.6)$$

for $k = 0,\ldots,M_d-1$, $j = 0,\ldots,N_d-1$ and $i = 0,\ldots,L_d-1$. The values M_d, N_d and L_d are the numbers of radial, azimuthal and axial points, respectively, needed to *de-alias* the computation up to the spectral order of $\mathbf{u}_{\rm S}$. For coarse grid computations, the convolution sums which appear when evaluating the non-linear terms may generate low *aliased* modes, (Canuto *et al.*, 1988). This phenomenon occurs when using a low resolution grid to compute the *Discrete Fourier Transform* (DFT) over the periodic axial or azimuthal domains. A similar problem arises in the non-periodic (radial) direction, although in this case it is related to a poorly resolved quadrature. One way to eliminate aliasing up to the established spectral order is the celebrated Orszag $\frac{3}{2}-$rule. For convective nonlinearitites, the aliasing error is eliminated up to order (L,N,M) if

$$L_d \geq \frac{3}{2}(2L+1)\,, \quad N_d \geq \frac{3}{2}(2N+1)\,, \quad M_d \geq 3M. \qquad (4.7)$$

The direct evaluation of (4.5) over each point of the grid (4.6) would require $O(LMN)$ operations. Overall, the total computation of $\mathbf{u}_{\rm S}$ would imply a total number of operations

of order $O(L^2N^2M^2)$. Nevertheless, we can substantially reduce the number of operations by means of the technique of *Partial Summation* (Boyd, 1999). We outline here the three basic steps.

(**I**. I) Evaluation over radial lines

We evaluate $\mathbf{u}_{\mathrm{S}}$ ($\mathbf{u}$ for simplicity) over the radial grid r_k:

$$\mathbf{u}_k(\theta,z)=\mathbf{u}(r_k,\theta,z)=\sum_{l=-L}^{L}\sum_{n=-N}^{N}\mathrm{e}^{\mathrm{i}(n\theta+2\pi lz/Q)}\underbrace{\sum_{m=0}^{M}a_{lnm}\mathbf{v}_{lnm}(r_k)}_{\alpha_{ln}^{(k)}},\quad (k=0,\ldots,M_d-1). \tag{4.8}$$

We have put a brace under the sum for the radial modes in (4.8) and we have identified it by the quantity $\alpha_{ln}^{(k)}$. The total number of operations needed to compute the α-coefficients is $O(M^2LN)$.

(**I**. II) Evaluation over radial – azimuthal planes

The second step is the evaluation of $\mathbf{u}_k(\theta,z)$ over the azimuthal grid

$$\mathbf{u}_{jk}(z)=\mathbf{u}(r_k,\theta_j,z)=\sum_{l=-L}^{L}\mathrm{e}^{\mathrm{i}2\pi lz/Q}\underbrace{\sum_{n=-N}^{N}\sum_{m=0}^{M}a_{lnm}\mathrm{e}^{\mathrm{i}n\theta_j}\mathbf{v}_{lnm}(r_k)}_{\beta_l^{(jk)}},\quad \left(\begin{array}{c} j=0,\ldots,N_d-1\\ k=0,\ldots,M_d-1\end{array}\right). \tag{4.9}$$

We take advantage of the first partial summation when computing the element $\beta_l^{(jk)}$ identified in (4.9) by means of the pre-computed $\alpha_{ln}^{(k)}$ coefficients

$$\beta_l^{(jk)}=\sum_{n=-N}^{N}\mathrm{e}^{\mathrm{i}n\theta_j}\sum_{m=0}^{M}a_{lnm}\mathbf{v}_{lnm}(r_k)=\sum_{n=-N}^{N}\mathrm{e}^{\mathrm{i}n\theta_j}\alpha_{ln}^{(k)}. \tag{4.10}$$

In this case, the number of operations required for the computation of the coefficients $\beta_l^{(jk)}$ is $O(N^2ML)$.

(**I**. III) Evaluation over radial – azimuthal – axial 3D grid

The last stage is the evaluation of $\mathbf{u}_{jk}(z)$ over the axial grid z_i

$$\mathbf{u}_{ijk}=\mathbf{u}(r_k,\theta_j,z_i)=\sum_{l=-L}^{L}\mathrm{e}^{\mathrm{i}2\pi lz_i/Q}\beta_l^{(jk)}=\left(\begin{array}{c}[v_r]_{ijk}\\ [v_\theta]_{ijk}\\ [v_z]_{ijk}\end{array}\right),\quad \left(\begin{array}{c} i=0,\ldots,L_d-1\\ j=0,\ldots,N_d-1\\ k=0,\ldots,M_d-1\end{array}\right), \tag{4.11}$$

which needs $O(L^2NM)$ operations.

Overall, the computational cost needed for the previous three stages is

$$O\big(LNM(L+N+M)\big), \tag{4.12}$$

to be compared with $O(L^2N^2M^2)$ for direct summation. The quantity appearing in (4.12) can be further improved by using the FFT in z and θ, and the FCT (*Fast Cosine Transform*) in r. In that case, the computational cost would be

$$O\big(LNM\ln(LNM)\big). \tag{4.13}$$

Nevertheless, we will make use of matrix multiplication in all the transformations. The reason is that although the FFT or FCT are more efficient when the dimension of the problem is high, for low moderate spatial resolution MM is still faster than on current processors (Boyd, 1999). Nevertheless, we emphasize that FCT is still applicable here and of very practical importance for future purposes such as high performance DNS simulation of fully developed turbulent flow.

(II) Evaluation of $\nabla\mathbf{u}_{\rm S}$ and product in physical space

The next step in the computation of $(\mathbf{u}_{\rm S}\cdot\nabla)\mathbf{u}_{\rm S}$ is to calculate the radial, azimuthal and axial derivatives of $\mathbf{u}_{ijk}$ given by (4.11) over the three dimensional grid (4.6). The azimuthal and axial derivatives are accomplished by means of the differentiation matrices $\mathbb{D}_\theta$ and $\mathbb{D}_z$ (see Appendix B), respectively, applied over the components of the velocity field obtained in (4.11),

$$[\partial_\theta v_r]_{ijk}=[\mathbb{D}_\theta]_{ii'}\,[v_r]_{i'jk}\ ,\quad [\partial_\theta v_\theta]_{ijk}=[\mathbb{D}_\theta]_{ii'}\,[v_\theta]_{i'jk}\ ,\quad [\partial_\theta v_z]_{ijk}=[\mathbb{D}_\theta]_{ii'}\,[v_z]_{i'jk}\,, \tag{4.14}$$

$$[\partial_z v_r]_{ijk}=[\mathbb{D}_z]_{jj'}\,[v_r]_{ij'k}\ ,\quad [\partial_z v_\theta]_{ijk}=[\mathbb{D}_z]_{jj'}\,[v_\theta]_{ij'k}\ ,\quad [\partial_z v_z]_{ijk}=[\mathbb{D}_z]_{jj'}\,[v_z]_{ij'k}\,. \tag{4.15}$$

For the radial derivative, we make use of the Chebyshev differentiation matrix $\mathbb{D}_r$, suitable for the half radial Gauss-Lobatto grid (see Appendix B). We apply partial summation techniques over the sum

$$\partial_r\mathbf{u}_{ijk}=\sum_{l=-L}^{L}\sum_{n=-N}^{N}\sum_{m=0}^{M}a_{lnm}\mathrm{e}^{\mathrm{i}(n\theta_j+2\pi lz_i/Q)}\mathrm{D}_r^{\otimes}\mathbf{v}_{lnm}(r_k), \tag{4.16}$$

where the operator $\mathrm{D}_r^{\otimes}$ is explicitly given in Appendix B. The computational cost of the radial, azimuthal and axial derivatives is given by the same quantity (4.12). Finally, we use the explicit expression of the nonlinear term in cylindrical coordinates (Tritton, 1988) for the computation of the point-to-point product

$$[(\mathbf{u}_{\rm S}\cdot\nabla)\mathbf{u}_{\rm S}]_{ijk}=\begin{pmatrix}[v_r]_{ijk}[\partial_r v_r]_{ijk}+[\frac{1}{r_k}][v_\theta]_{ijk}[\partial_\theta v_r]_{ijk}+[v_z]_{ijk}[\partial_z v_r]_{ijk}-[\frac{1}{r_k}][v_\theta]^2_{ijk}\\ [v_r]_{ijk}[\partial_r v_\theta]_{ijk}+[\frac{1}{r_k}][v_\theta]_{ijk}[\partial_\theta v_\theta]_{ijk}+[v_z]_{ijk}[\partial_z v_\theta]_{ijk}+[\frac{1}{r_k}][v_\theta]_{ijk}[v_r]_{ijk}\\ [v_r]_{ijk}[\partial_r v_z]_{ijk}+[\frac{1}{r_k}][v_\theta]_{ijk}[\partial_\theta v_z]_{ijk}+[v_z]_{ijk}[\partial_z v_z]_{ijk}\end{pmatrix}. \tag{4.17}$$

(III) Projection onto Fourier-Chebyshev space

The nonlinear term b_{lnm} appearing in (3.10) is the projection of $(\mathbf{u}_{\rm S}\cdot\nabla)\mathbf{u}_{\rm S}$ over the dual space spanned by the $\mathbf{\Psi}_{lnm}$ functions defined in (3.5),

$$b_{lnm}=(\mathbf{\Psi}_{lnm}\ ,\ (\mathbf{u}_{\rm S}\cdot\nabla)\mathbf{u}_{\rm S})=\int_0^Q\mathrm{d}z\int_0^{2\pi}\mathrm{d}\theta\int_0^1 r\mathrm{d}r\ \mathrm{e}^{-\mathrm{i}(2\pi lz/Q+n\theta)}\tilde{\mathbf{v}}_{lnm}\cdot[(\mathbf{u}_{\rm S}\cdot\nabla)\mathbf{u}_{\rm S}]. \tag{4.18}$$

The volume integral in (4.18) involves two Fourier transforms in z and θ and a Chebyshev transform in r. The former two can be exactly calculated by means of matrix multiplication and the last one by means of Gauss-Lobatto quadrature, although the FCT is also an alternative. For that purpose, we use the values $[(\mathbf{u}_S \cdot \nabla)\mathbf{u}_S]_{ijk}$ previously computed in (4.17). The discrete version of the Fourier-Chebyshev transform (4.18) is

$$b_{lnm} = \sum_{i=0}^{L_d-1} \sum_{j=0}^{N_d-1} \sum_{k=0}^{M_d-1} \mathrm{e}^{-\mathrm{i}(n\theta_j + 2\pi l z_i/Q)}\; r_k\; w_k\; \tilde{\mathbf{v}}_{lnm}(r_k)\; [(\mathbf{u}_S \cdot \nabla)\mathbf{u}_S]_{ijk}\;, \qquad \begin{pmatrix} l = -L, \ldots, L \\ n = -N, \ldots, N \\ m = 0, \ldots, M \end{pmatrix}, \tag{4.19}$$

where w_k are the Gauss-Lobatto weight coefficients for the quadrature in the radial direction. The direct evaluation of the sum (4.19) would require $O(L^2N^2M^2)$ operations. For computational efficiency we use partial summation techniques.

5 Validation of the numerical scheme

5.1 Convergence analysis

The spatial convergence of the Petrov-Galerkin method was already tested in (Meseguer & Trefethen, 2000) for linear stability analysis. The method provided spectral accuracy in all cases studied. For the nonlinear time-dependent problem, we have solved the same initial value problem by means of three different schemes. In all cases, we have considered the same spectral resolution in space, the same initial condition for the amplitudes and the total time in the integrations. Figure 3 captures the essential features of the convergence of the three different time marching schemes. The first one, **SS**2, is the 2nd order linear-nonlinear Strang Splitting. The second and third ones, **BD2AB2** and **BD4AB4**, are the second and fourth order Backwards Difference / Adams-Bashforth methods, respectively. The plot represents the absolute error of the Fourier coefficients $a_{lnm}^{\Delta t}(T)$ in the L_2-norm

$$\|\epsilon(\Delta t)\|_2 = \left(\sum_{l,n,m} \mid a_{lnm}^{\Delta t}(T) - a_{lnm}^{\Delta t_0}(T) \mid^2 \right)^{1/2}, \tag{5.1}$$

at the end of the run ($t = T = 50$), as a function of Δt, where the reference time step is $\Delta t_0 = 6.6 \cdot 10^{-3}$.

As mentioned in the overview, we also considered **ETD** schemes for the integration of the problem. These schemes have been succesfully applied in one-dimensional nonlinear PDEs, at least when the structure of the linear operator is diagonal and nonsingular (Cox & Matthews, 2001). Even though our linear operator is nonsingular, its eigenvalues are very close to the origin and the resulting exponential time differencing mappings are not well-conditioned. To sum up, we conclude that linearly implicit methods such as **BD4AB4** are the most suitable for the time integration of this problem. Henceforth, all the computations presented will be carried out with the **BD4AB4** scheme.

6 Comparison with previous works: streamwise streaks

In this section, we study the nonlinear evolution of streamwise independent perturbations. This evolution has been studied recently by (Zikanov, 1996). Zikanov analyzed the nonlinear

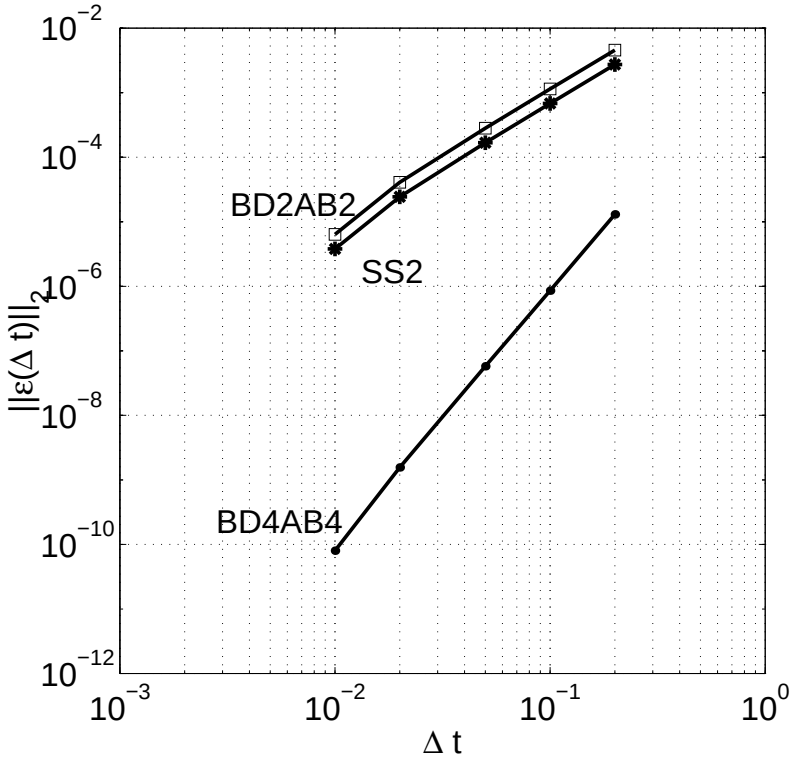

Figure 3: Absolute error (5.1) for the three different time marching schemes. The three curves represent the error obtained for the same initial value problem in the interval $t \in [0, 50]$. In all three cases, the spectral resolution was the same: $M = 6$, $N = 5$, $L = 0$.

evolution of perturbations independent of the streamwise coordinate. From the equation of the perturbation (2.11), it is straightforward to see that an initial streamwise independent field remains independent of z for all time $t > 0$, i.e., the nonlinear terms preserve their streamwise symmetry.

We define the *energy* of an arbitrary vector field $\mathbf{u}$ as the inner product

$$\mathrm{E}(\mathbf{u}) = \frac{1}{2}\int_0^Q \mathrm{d}z \int_0^{2\pi} \mathrm{d}\theta \int_0^1 r\mathrm{d}r\ \mathbf{u}^* \cdot \mathbf{u}. \tag{6.1}$$

With the previous definition, a straightforward calculation leads to the energy of the Hagen-Poiseuille flow,

$$\mathrm{E}_{\mathrm{HP}} = \frac{\pi}{6}Q. \tag{6.2}$$

Henceforth, we will normalize the energy of the perturbations with respect to the basic quantity E_{HP}. We define the *relative energy*, or more briefly just "energy", of an arbitrary perturbation $\mathbf{u}$ as the ratio

$$\boldsymbol{\varepsilon}(\mathbf{u}) = \frac{\mathrm{E}(\mathbf{u})}{\mathrm{E}_{\mathrm{HP}}}\ . \tag{6.3}$$

For the comparison with the computations carried out by Zikanov we consider a perturbation of energy ε_0 with initial condition $\mathbf{u}_S^0$ in (3.14), which is prescribed by the amplitudes

$$a_{lnm}^0 \;=\; a_{lnm}(t=0) \;=\; \left\{ \begin{array}{ll} A_0 & l=0,\; n=\pm 1,\; m=0 \\ 0 & \text{otherwise} \end{array} \right\} \tag{6.4}$$

where A_0 is a real constant such that $\varepsilon(\mathbf{u}_S^0) = \varepsilon_0$. This is equivalent to considering the simplest non-axisymmetric streamwise-independent field, with azimuthal wavenumber $n = 1$. Following Zikanov's specifications, we have computed the evolution of the initial condition (6.4) for different initial energies. In figure 4 we have plotted the $\mathrm{G}(t)$ growth factor of the perturbation, defined as

$$\mathrm{G}(t) = \frac{\varepsilon(t)}{\varepsilon_0}. \tag{6.5}$$

This quantity has been originally considered in (Boberg & Brosa, 1988) and (Schmid & Henningson, 1994) in the transient growth analysis of pipe flow.

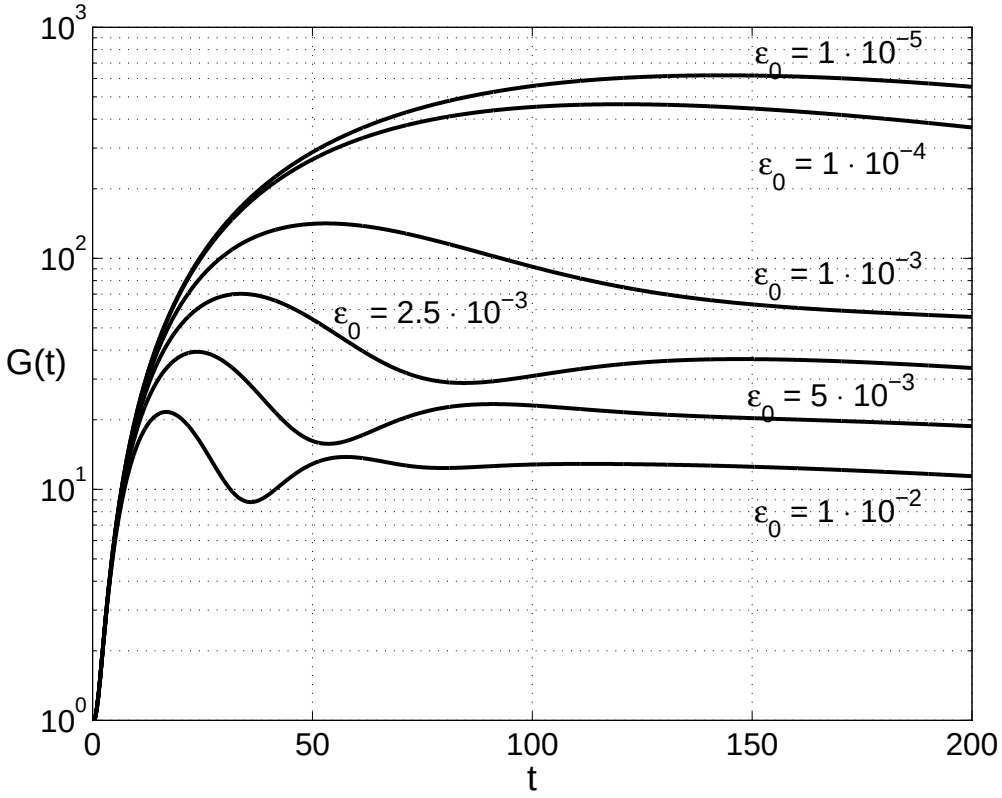

Figure 4: Growth factor $\mathrm{G}(t)$ for different initial energies for $\mathrm{Re} = 3000$. This plot was generated using $N = 9$ azimuthal modes, $M = 6$ radial modes and $\Delta t = 0.1$, but further experiments show that it is converged to plotting accuracy.

In all cases studied, the agreement with Zikanov's computations is very good (see figure 5). As long as the initial energy goes to zero, the nonlinear effects become negligible and the dynamics is governed by the linear nonnormal mechanism. This is clearly seen in the top

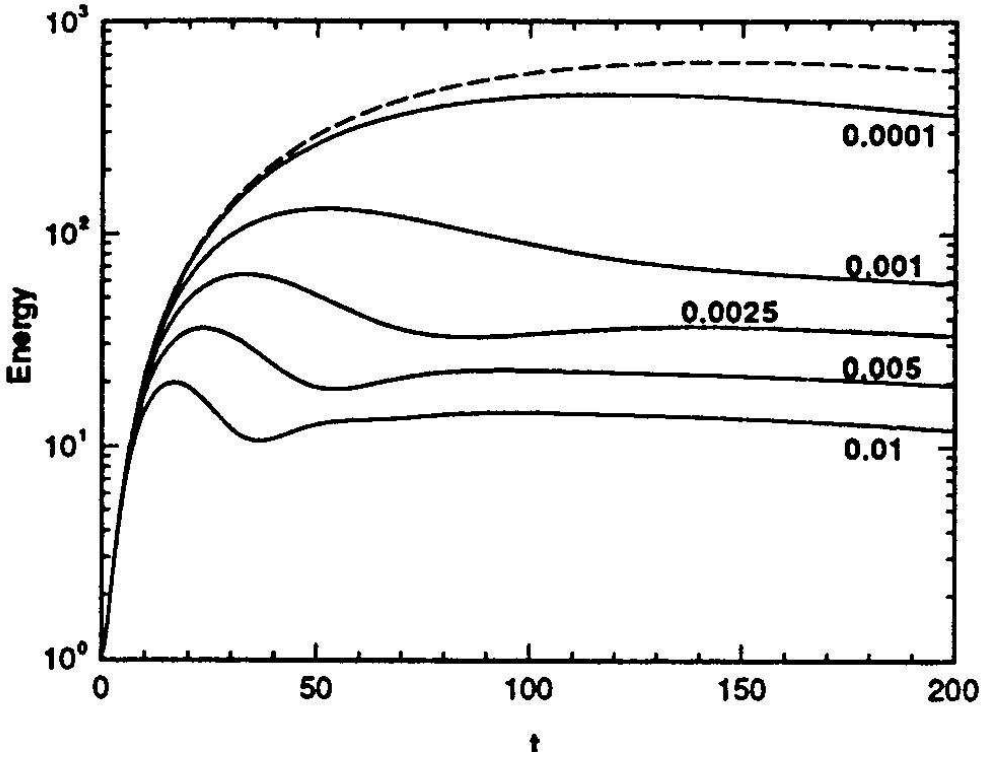

Figure 5: Original figure from (Zikanov, 1996). Energy growth factor G(t) for Re = 3000. The initial energies are the same as in figure 4. The numerical method for these computations was a hybrid 2nd order finite differences scheme in r combined with spectral Fourier method in θ. For the time integration, Zikanov made use of a first order implicit Euler method for the linear terms and a second order explicit Adams-Bashforth for the nonlinear part.

curve (for $\varepsilon_0 = 1 \cdot 10^{-5}$), where the amplification factor reaches a maximum value of G ~ 620 for $t \sim 143$. This is in agreement with the former linear analysis carried out in (Schmid & Henningson, 1994) or in (Meseguer & Trefethen, 2000), where the maximum amplification factor was $G_{max} \sim 649$ for $t \sim 147$. In figure 6 we have plotted the modulated axial flow, $w_B + w_S$, at $t = 0$, $t = 17$, $t = 75$ and $t = 150$, for $\varepsilon_0 = 1 \cdot 10^{-2}$. Figure 7 recovers the computations carried out by Zikanov for the same initial energy and Reynolds number. We can observe the formation of streaks by the lift-up effect, where high speed axial flow is driven to low axial speed regions near the wall (Landahl, 1980). By the same rule, the axial speed of the flow at the axis is considerably diminished (see, figure 8). The first important feature of this transient flow is the presence of saddle points in its profile. This would lead to an inviscid instability when perturbing the flow with three-dimensional disturbances. The second is that this transient regime is almost steady, as we observe more clearly from the bottom curve in figure 4, where the amplitude of the perturbation is almost constant for a long period of time. Nevertheless, this "long term" behaviour is only apparent. In a typical experiment (Darbyshire & Mullin, 1995), where $\nu = 1 \cdot 10^{-2}$ cm$^2 \cdot$ s^{-1} (water) and $a = 1$ cm (pipe radius),

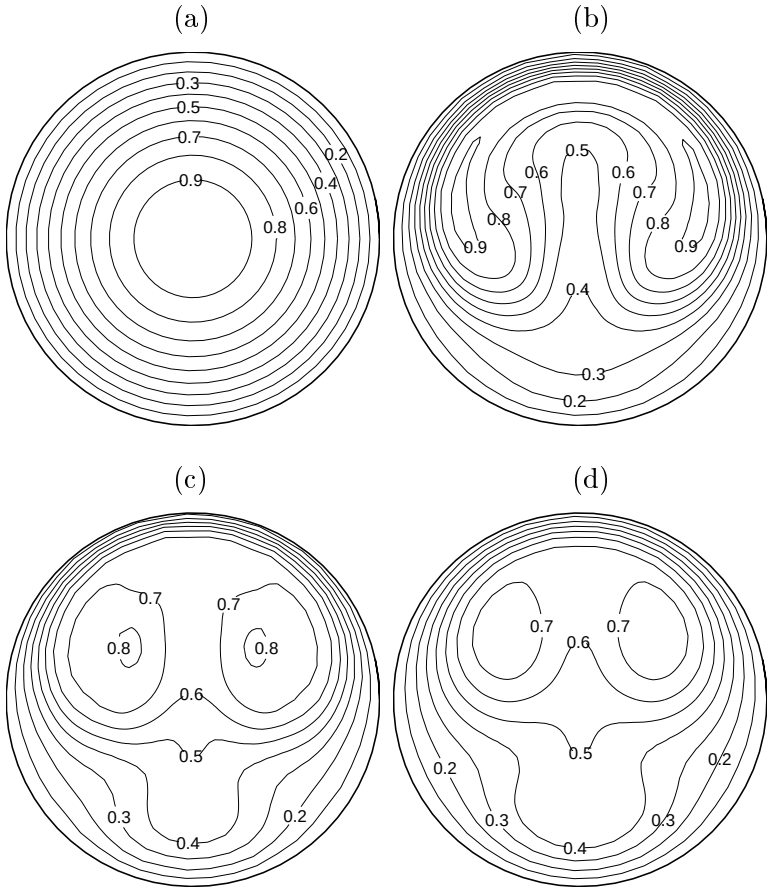

Figure 6: Formation of streaks for the Re = 3000 and $\varepsilon_0 = 1 \cdot 10^{-2}$. Modulated axial flow $w_{\mathrm{B}} + w_{\mathrm{S}}$ at: (a) $t = 0$, (b) $t = 17$, (c) $t = 75$ and (d) $t = 150$.

the dimensional unit of time is

$$\tau = \frac{a}{U_{\mathrm{CL}}} \text{ s.} = \frac{a^2}{\nu \mathrm{Re}} \text{ s.} \sim \frac{1}{\mathrm{Re}/100} \text{ s.},$$

where

$$(\Delta t)_{\text{dimensional}} = \tau \ (\Delta t)_{\text{nondimensional}}. \tag{6.6}$$

Therefore, the streaks appearing in figure 6d, for nondimensional time $t = 150$, would actually appear after 5 seconds in the experiments, approximately. This feature provides the flow the property of being potentially unstable when infinitesimal SDV perturbations are present. This stability analysis can be carried out by linearizing the Navier-Stokes equations in a neighbourhood of the transient modulated 2D-flow. This is Zikanov's approach; he studied the linear evolution of three-dimensional perturbations once the streaks were already developed. Zikanov observed transient exponential growth of SDV for some range of axial wavenumbers. This is a clear indication that the transient flow is linearly unstable and that this mechanism may eventually lead to turbulent regimes.

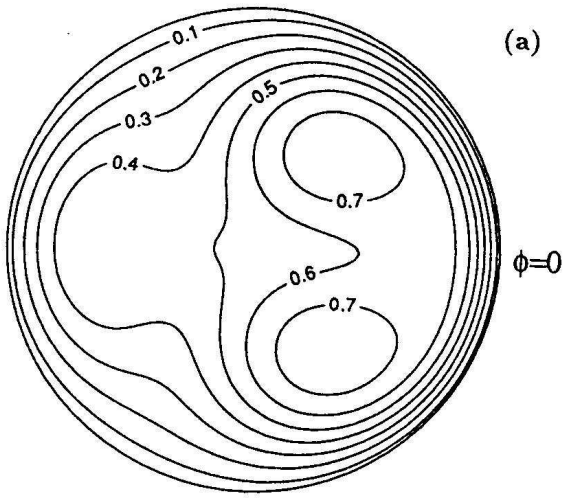

Figure 7: Original figure taken from (Zikanov, 1996). Modulated axial flow at $t = 150$ and $\epsilon_0 = 1 \cdot 10^{-2}$, for Re = 3000. Compare with figure 6(d).

7 Streak breakdown

In this section we study the nonlinear evolution of three-dimensional perturbations. For this purpose, we consider the same kind of two-dimensional streamwise-independent disturbances considered in the previous section. In order to trigger instability of the streaks generated by the two-dimensional vortices, we add smaller three-dimensional SDV perturbations and we explore the potential destabilization of the flow as a function of the 2D and 3D energies. The initial condition that we consider in this case is

$$a^0_{lnm} \;=\; a_{lnm}(t=0) \;=\; \left\{ \begin{array}{ll} A_0 & l=0,\ n=\pm 1,\ m=0 \\ A_1 & l=\pm 1,\ n=0,\ \pm 1,\ m=0 \\ 0 & \text{otherwise} \end{array} \right\}, \tag{7.1}$$

where A_0 and A_1 are suitable real constants so that the energy of the 2D and 3D modes is distributed as follows:

$$\varepsilon(\mathbf{\Phi}_{0\,n\,0}) = \varepsilon_0^{2\mathrm{D}},\ \text{for } n=\pm 1, \quad \text{and} \quad \varepsilon(\mathbf{\Phi}_{\pm 1\,n\,0}) = \varepsilon_0^{3\mathrm{D}},\ \text{for } n=0,\ \pm 1, \tag{7.2}$$

for prescribed values $\varepsilon_0^{2\mathrm{D}}$ and $\varepsilon_0^{3\mathrm{D}}$. In figures 9 and 10, we have plotted the time evolution of the energies corresponding to the streamwise-independent ($\varepsilon^{2\mathrm{D}}$) and SDV ($\varepsilon^{3\mathrm{D}}$). The computations have been made for Reynolds numbers increasing from Re = 1000 to Re = 3000. In each case, three independent integrations have been carried out, always starting with $\varepsilon_0^{2\mathrm{D}} = 1 \cdot 10^{-2}$ and $\varepsilon_0^{3\mathrm{D}} = 1 \cdot 10^{-4}$, $\varepsilon_0^{3\mathrm{D}} = 1 \cdot 10^{-6}$ or $\varepsilon_0^{3\mathrm{D}} = 1 \cdot 10^{-8}$. For Re = 1000 (figure 9, top), the streaks do not appear, and the two and three dimensional energies decay. We observe that the three-dimensional perturbations evolve almost identically in the three independent integrations. This is because the nonlinearities are still negligible at that stage and the evolution mechanism is basically linear. For Re = 2000 (figure 9, bottom), the streaks already appear and we observe for the first time the instability of the three-dimensional perturbation for the case $\varepsilon_0^{3\mathrm{D}} = 1 \cdot 10^{-4}$.

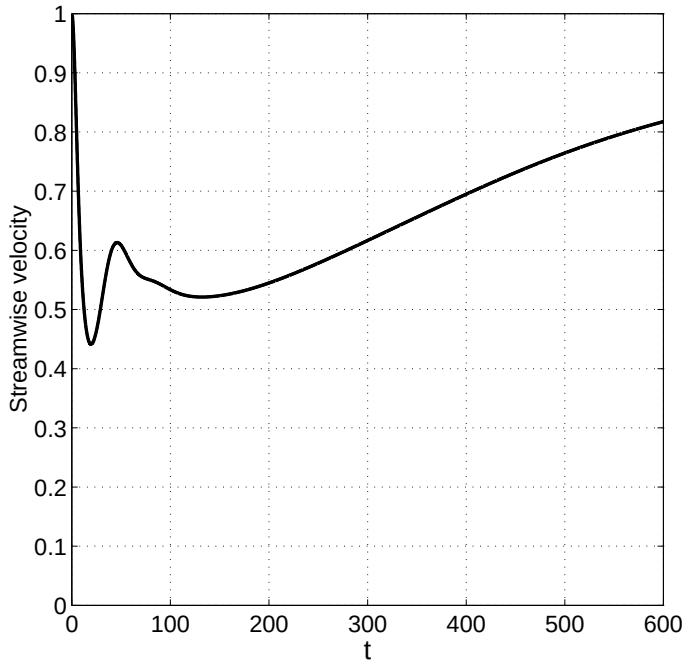

Figure 8: Time evolution of the axial velocity at the center axis for $\varepsilon_0 = 1 \cdot 10^{-2}$, Re = 3000. The computation corresponds to the same time evolution carried out in figure 6.

Nevertheless, this destabilization is only transient and the perturbations eventually decay. For Re = 2500 (figure 10, top), only the smallest SDV, for $\varepsilon_0^{3D} = 1 \cdot 10^{-8}$, is not able to destabilize the streak. The other two initial conditions clearly trigger transition. Finally, for Re = 3000 (figure 10, bottom), all the SDV disturbances suffer an exponential instability, leading always to the streak breakdown phenomenon. In figure 11, we have carried out another computation for higher Reynolds number, Re = 4000, and lower amplitude of the initial perturbation $\varepsilon_0^{2D} = 1 \cdot 10^{-3}$. In the first case (top figure 11), we see that three independent streamwise dependent perturbations of energies $\varepsilon_0^{3D} = 1 \cdot 10^{-10,\,-9,\,-8}$, are not strong enough to destabilize the streak. The threshold energy for this instability mechanism is of order 10^{-7}, see figure 11, bottom. In figure 12 we have represented the axial velocity of the flow at the center of the pipe for Re = 5000. In the initial stages, we observe a similar behaviour to the evolution seen in figure 8. The differences appear as soon as the axial velocity has decreased approximately by 50%. Occasionally, this chaotic evolution may eventually decay. We should enhance the time integration interval in order to decide whether what is observed is actually a transition to turbulence or not. This problem not only arises in the numerical integrations, but also in the experiments, where turbulent structures may be advected downstream and leave the pipe, making it impossible to determine whether the flow is laminar or turbulent. To confirm the existence of an strange attractor, different dynamical aspects of the problem such as Liapunov exponents, Fourier-time analysis or Poincaré sections should be studied (Wiggins, 1990). It has been suggested that turbulence (or chaotic evolution) in pipe flow, even for relatively high Reynolds numbers, is only a transient phenomenon (Brosa, 1989). In any case, the answer to all these questions is far beyond our purposes in this work.

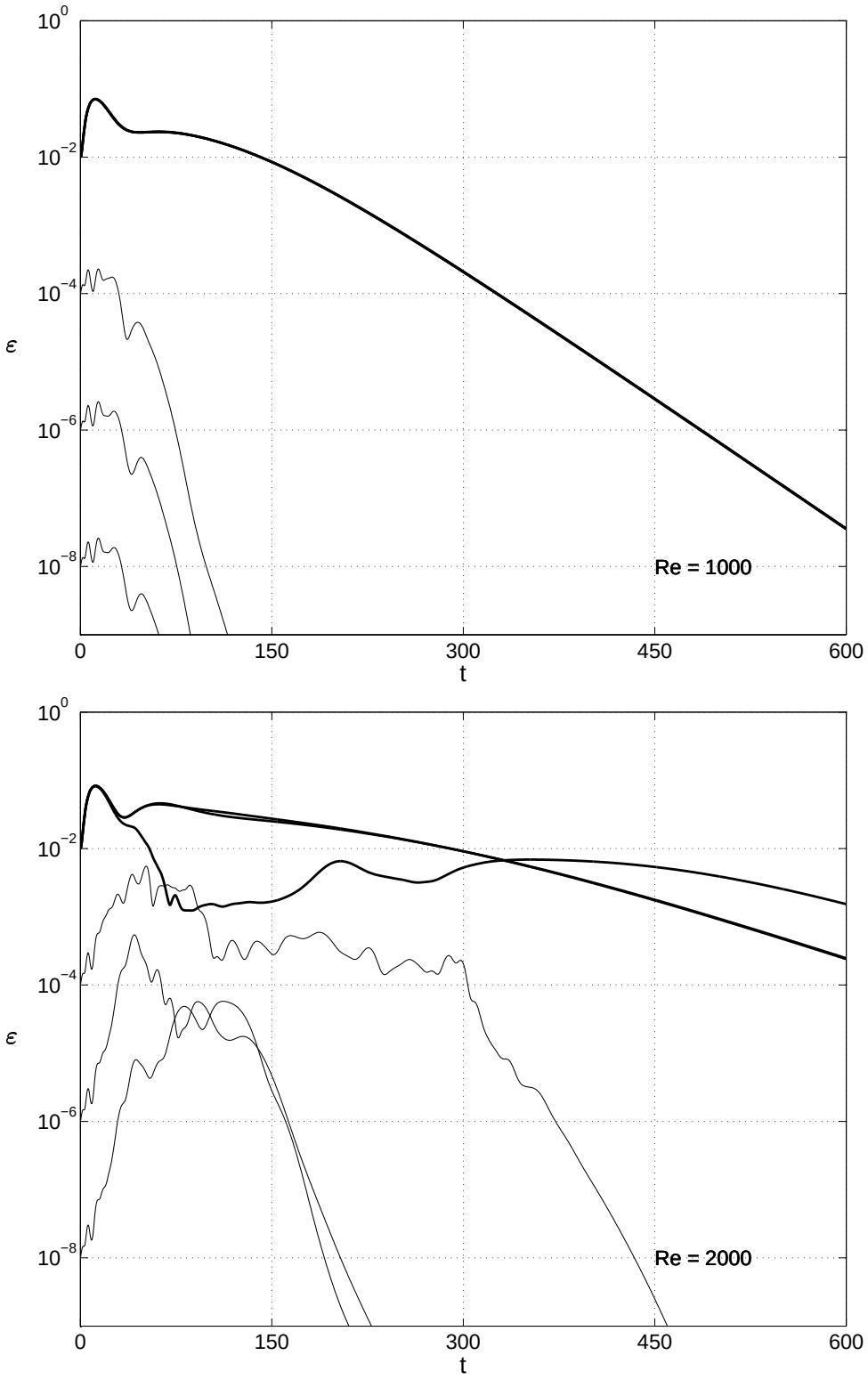

Figure 9: Time evolution of the energy of 2D (thick curves) and 3D (thin curves) perturbations for different values of Re. For these computations, the aspect ratio was $Q = \pi$ (i.e., the lowest nonzero axial wavenumber is $k = 2$). We used $M = 14$ modes in r, $N = 7$ in θ and $L = 1$ in z. The time step is $\Delta t = 5 \cdot 10^{-2}$. In each one of the cases, we have not found any qualitative difference when increasing the spectral order.

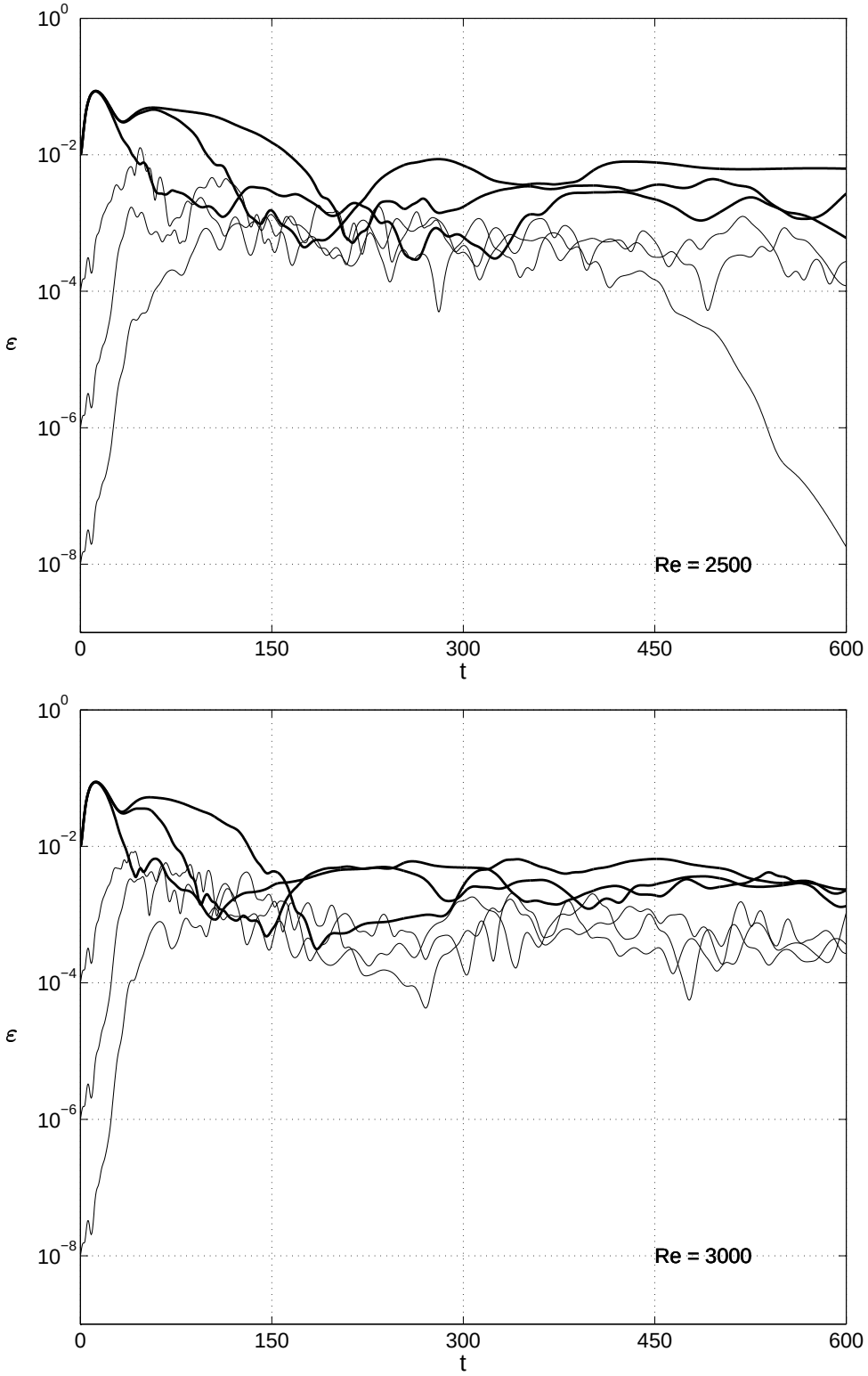

Figure 10: Same as figure 9, for Re = 2500, 3000.

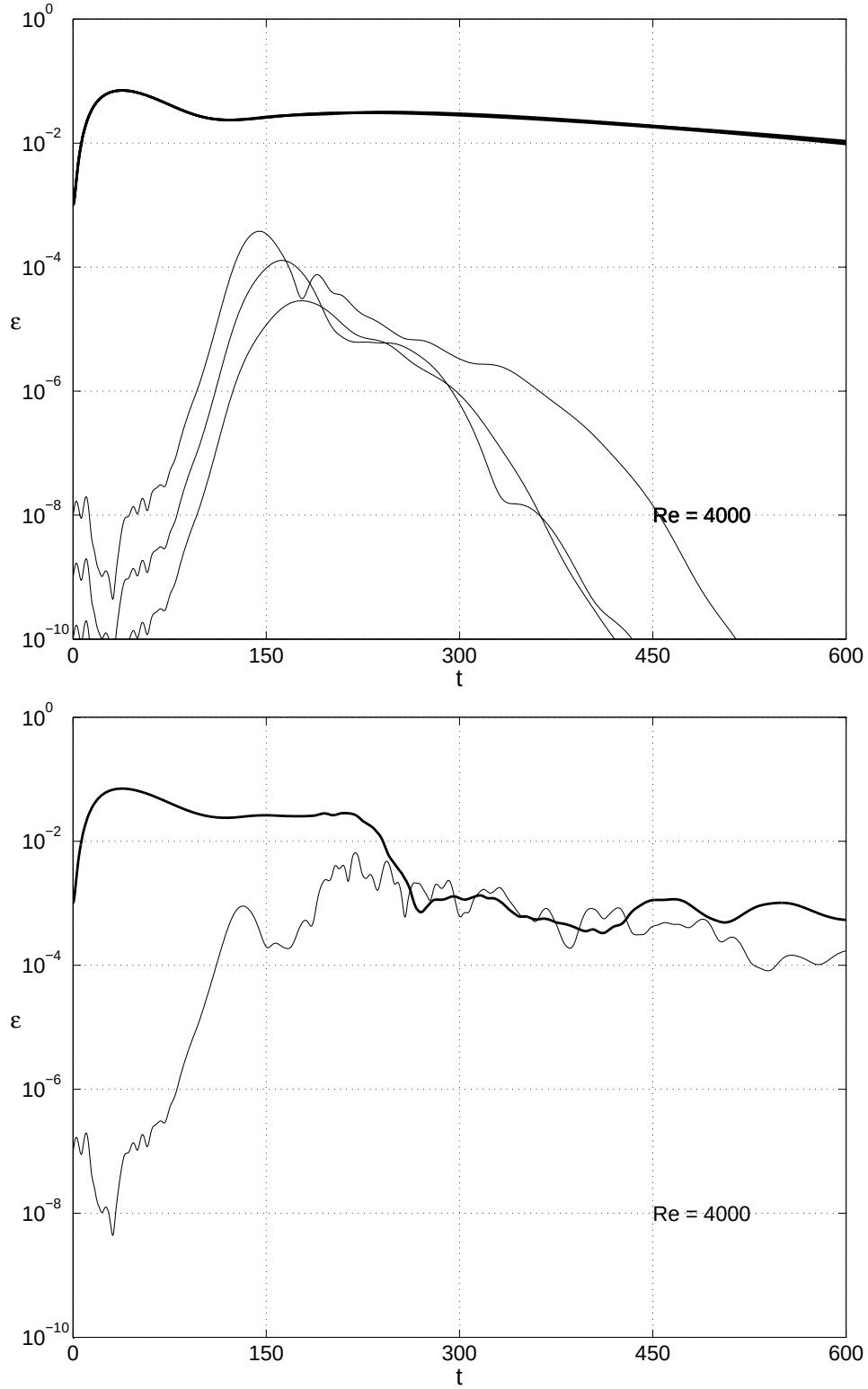

Figure 11: Time evolution of the energy of 2D (thick curves) and 3D (thin curves) perturbations for Re = 4000. At the top, the three-dimensional perturbations are too weak to destabilize the streak. At the bottom, a three-dimensional perturbation of energy 10^{-7} triggers instability. The spectral and time resolution in these computation was the same as in figures 9 and 10.

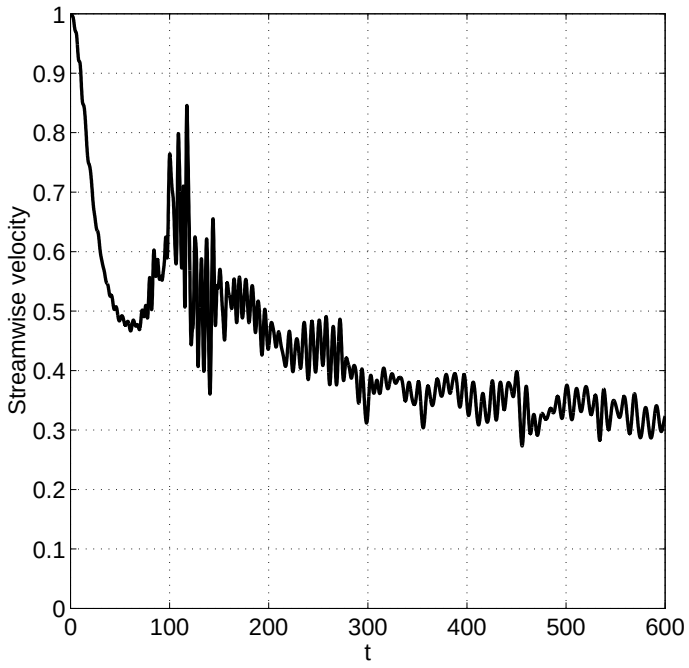

Figure 12: Axial velocity at the center line for $\varepsilon_0^{2D} = 1 \cdot 10^{-3}$, $\varepsilon_0^{3D} = 1 \cdot 10^{-5}$, Re = 5000.

8 Conclusions

A three-dimensional unsteady solenoidal spectral method has been developed in cylindrical coordinates for the numerical study of linear and nonlinear transitional dynamics in pipe flows. A pseudospectral algorithm has been developed for the efficient computation of the nonlinear terms. Different time integration schemes have been tested. Linearly implicit methods seem to be the most suitable to deal with the stiffness of the equations. The algorithm provides spectral accuracy in space and fourth order accuracy in time. The numerical results for the nonlinear evolution of streamwise perturbations are in a very good agreement with previous works. The stability of the transient two-dimensional flows has been studied by perturbing those structures with very small three-dimensional disturbances. Even for coarse spatial resolution, the results are consistent with the streak breakdown process which is found in other subcritical shear flows.

ACKNOWLEDGMENTS

This research was supported by the Engineering and Physical Sciences Research Council of the United Kingdom under Grant GR/M30890.

Appendix A Solenoidal bases

In what follows, we define

$$\mathrm{h}_m(r) = (1-r^2)\mathrm{T}_{2m}(r), \quad \mathrm{g}_m(r) = (1-r^2)\mathrm{h}_m(r), \quad \mathrm{D} = \frac{\mathrm{d}}{\mathrm{d}r}, \quad \mathrm{D}_+ = \mathrm{D} + \frac{1}{r} \qquad \text{(A.1)}$$

where T_{2m} is the Chebyshev polynomial of degree $2m$ and $r \in (0,1)$. We begin with the *trial* functions $\mathbf{\Phi}_{lnm}(r,\theta,z)$, distinguishing two cases depending on whether n is zero or nonzero.

Case $n = 0$. The basis is spanned by the elements

$$\mathbf{\Phi}^{(1)}_{l0m} = \mathrm{e}^{\,\mathrm{i}\,\frac{2\pi}{Q} l\, z}\mathbf{v}^{(1)}_{lnm} = \mathrm{e}^{\,\mathrm{i}\,\frac{2\pi}{Q} l\, z}\begin{pmatrix} 0 \\ r\mathrm{h}_m(r) \\ 0 \end{pmatrix}, \tag{A.2}$$

$$\mathbf{\Phi}^{(2)}_{l0m} = \mathrm{e}^{\,\mathrm{i}\,\frac{2\pi}{Q} l\, z}\mathbf{v}^{(2)}_{lnm} = \mathrm{e}^{\,\mathrm{i}\,\frac{2\pi}{Q} l\, z}\begin{pmatrix} -\frac{2\pi}{Q}\mathrm{i}\; l\; r\mathrm{g}_m(r) \\ 0 \\ \mathrm{D}_+[r\mathrm{g}_m(r)] \end{pmatrix}, \tag{A.3}$$

except that if $l = 0$, the third component of $\mathbf{\Phi}^{(2)}_{lnm}$ is replaced by $\mathrm{h}_m(r)$.

Case $n \neq 0$. In this case, the basis is spanned by the elements

$$\mathbf{\Phi}^{(1)}_{lnm} = \mathrm{e}^{\mathrm{i}(n\;\theta + \frac{2\pi}{Q} l\; z)}\mathbf{v}^{(1)}_{lnm} = \mathrm{e}^{\mathrm{i}(n\;\theta + \frac{2\pi}{Q} l\; z)}\begin{pmatrix} -\mathrm{i}\; n\; r^{\sigma-1}\; \mathrm{g}_m(r) \\ \mathrm{D}[r^{\sigma}\; \mathrm{g}_m(r)] \\ 0 \end{pmatrix}, \tag{A.4}$$

$$\mathbf{\Phi}^{(2)}_{lnm} = \mathrm{e}^{\mathrm{i}(n\;\theta + \frac{2\pi}{Q} l\; z)}\mathbf{v}^{(2)}_{lnm} = \mathrm{e}^{\mathrm{i}(n\;\theta + \frac{2\pi}{Q} l\; z)}\begin{pmatrix} 0 \\ -\mathrm{i}\frac{2\pi}{Q}\; l\; r^{\sigma+1}\; \mathrm{h}_m(r) \\ \mathrm{i}\; n\; r^{\sigma}\mathrm{h}_m(r) \end{pmatrix}, \tag{A.5}$$

where, following the regularization rules proposed in (Priymak & Miyazaki, 1998),

$$\sigma = \begin{cases} 2 & (n \text{ even}) \\ 1 & (n \text{ odd}). \end{cases} \tag{A.6}$$

Mathematically speaking, the pure imaginary factors in $\mathbf{\Phi}^{(2)}_{lnm}$ could be dispensed with, but we leave them in so that the basis functions have a desirable symmetry property: if l and n are negated, each basis function is replaced by its complex conjugate, i.e.,

$$\left[\mathbf{\Phi}^{(1,2)}_{lnm}\right]^* = \mathbf{\Phi}^{(1,2)}_{-l,\,-n,\;m} \quad . \tag{A.7}$$

For the *test* functions $\mathbf{\Psi}_{lnm}(r,\theta,z)$, we could take the same basis. However, the resulting matrices appearing in (3.11) and (3.12) would be dense, whereas they can be made to be banded if one chooses the projection bases as follows.

Case $n = 0$.

$$\begin{aligned} \mathbf{\Psi}^{(1)}_{l0m} &= \mathrm{e}^{\,\mathrm{i}\,\frac{2\pi}{Q} l\, z}\tilde{\mathbf{v}}^{(1)}_{l0m}(r) = \mathrm{e}^{\,\mathrm{i}\,\frac{2\pi}{Q} l\, z}\begin{pmatrix} 0 \\ \mathrm{h}_m(r) \\ 0 \end{pmatrix}\frac{1}{\sqrt{1-r^2}}, \\ \mathbf{\Psi}^{(2)}_{l0m} &= \mathrm{e}^{\,\mathrm{i}\,\frac{2\pi}{Q} l\, z}\tilde{\mathbf{v}}^{(2)}_{l0m}(r) = \mathrm{e}^{\,\mathrm{i}\,\frac{2\pi}{Q} l\, z}\begin{pmatrix} -\frac{2\pi}{Q}\mathrm{i}\; l\; r^2\mathrm{g}_m(r) \\ 0 \\ \mathrm{D}_+[r^2\mathrm{g}_m(r)] + r^3\; \mathrm{h}_m(r) \end{pmatrix}\frac{1}{\sqrt{1-r^2}}, \end{aligned} \tag{A.8}$$

except that the third component of the vector in $\mathbf{\Psi}^{(2)}_{l0m}$ is replaced by $r\,\mathrm{h}_m(r)$ if $l=0$.

Case $n \neq 0$.

$$\begin{aligned}
\mathbf{\Psi}^{(1)}_{lnm} &= \mathrm{e}^{\mathrm{i}(n\,\theta+\frac{2\pi}{Q}l\,z)}\tilde{\mathbf{v}}^{(1)}_{lnm}(r) = \mathrm{e}^{\mathrm{i}(n\,\theta+\frac{2\pi}{Q}l\,z)}\begin{pmatrix} \mathrm{i}\,n\,r^{\beta}\mathrm{g}_m(r) \\ \mathrm{D}[r^{\beta+1}\,\mathrm{g}_m(r)] + r^{\beta+2}\mathrm{h}_m(r) \\ 0 \end{pmatrix}\frac{1}{\sqrt{1-r^2}}, \\
\mathbf{\Psi}^{(2)}_{lnm} &= \mathrm{e}^{\mathrm{i}(n\,\theta+\frac{2\pi}{Q}l\,z)}\tilde{\mathbf{v}}^{(2)}_{lnm}(r) = \mathrm{e}^{\mathrm{i}(n\,\theta+\frac{2\pi}{Q}l\,z)}\begin{pmatrix} 0 \\ -\frac{2\pi}{Q}\mathrm{i}\,l\,r^{\beta+2}\mathrm{h}_m(r) \\ \mathrm{i}\,n\,r^{\beta+1}\,\mathrm{h}_m(r) \end{pmatrix}\frac{1}{\sqrt{1-r^2}},
\end{aligned} \tag{A.9}$$

except that the third component of the vector in $\mathbf{\Psi}^{(2)}_{lnm}$ is replaced by $r^{1-\beta}\mathrm{h}_m(r)$ if $l=0$, where

$$\beta = \begin{cases} 0 & (n \text{ even}) \\ 1 & (n \text{ odd}). \end{cases} \tag{A.10}$$

These vector fields include the Chebyshev factor $(1-r^2)^{-1/2}$ so that the products between the test and trial functions can be exactly calculated via Gauss-Lobatto quadrature, leading to banded matrices. We note that the radial variable runs from 0 to 1, and not from -1 to 1, as would expected by using Chebyshev polynomials.

Appendix B Differentiation matrices

In the radial coordinate, we consider the *Gauss-Lobatto* points

$$r_k = -\cos\left(\frac{\pi k}{N}\right), \quad k = 0,\ldots,N, \tag{B.1}$$

where we will assume that N is *odd*. The spectral differentiation matrix is given by

$$(\mathbb{D}_r)_{ij} = \begin{cases} (1+2N^2)/6 & i=j=N \\ -(1+2N^2)/6 & i=j=0 \\ -\dfrac{x_i}{2(1-x_i^2)} & i=j\ ;\ 0<i<N \\ (-1)^{i+j}\,\dfrac{c_j}{c_i(x_j-x_i)} & i\neq j \end{cases}, \tag{B.2}$$

where $c_j = 1$ for $0 < j < N$ and $c_0 = c_N = 2$, see (Boyd, 1999) or (Trefethen, 2000). The vector functions $\mathbf{\Phi}^{(1,2)}_{lnm}$ satisfy certain parity properties in the radial variable discretized in (B.1). The radial, azimuthal and axial components are either *even* or *odd* functions of r. Therefore, we only need to consider the positive part of the grid

$$r_k^{+} = -\cos\left(\frac{\pi k}{N}\right), \quad k = \frac{N+1}{2},\ldots,N. \tag{B.3}$$

For arbitrary even, $\mathrm{f_e}(r)$, or odd, $\mathrm{f_o}(r)$, functions satisfying

$$\mathrm{f_e}(r_k) = \mathrm{f_e}(r_{N-k}), \quad \mathrm{f_o}(r_k) = -\mathrm{f_o}(r_{N-k}), \qquad k = 0, \ldots, \frac{N-1}{2}, \tag{B.4}$$

the differentiation matrices which provide the first derivatives

$$\left(\frac{\mathrm{df_e}}{\mathrm{d}r}\right)_{r=r_i^+} = (\mathbb{D}_r^{\mathrm{e}})_{ij}\ \mathrm{f_e}(r_j^+), \quad \left(\frac{\mathrm{df_o}}{\mathrm{d}r}\right)_{r=r_i^+} = (\mathbb{D}_r^{\mathrm{o}})_{ij}\ \mathrm{f_o}(r_j^+), \tag{B.5}$$

are obtained from the Chebyshev matrix (B.2):

$$(\mathbb{D}_r^{\mathrm{e}})_{ij} = (\mathbb{D}_r)_{ij} + (\mathbb{D}_r)_{i\,N-j}, \quad (\mathbb{D}_r^{\mathrm{o}})_{ij} = (\mathbb{D}_r)_{ij} - (\mathbb{D}_r)_{i\,N-j}, \quad i,j = \frac{N+1}{2}, \ldots, N. \tag{B.6}$$

The radial derivative of an arbitrary element $\mathbf{v}_{lnm}(r)$ of the trial basis is given by

$$\frac{\mathrm{d}}{\mathrm{d}r}\mathbf{v}_{lnm}(r) = \mathbb{D}_r^{\otimes}\ \mathbf{v}_{lnm}(r), \tag{B.7}$$

where

$$\mathbb{D}_r^{\otimes} = \begin{pmatrix} \mathbb{D}_r^{\mathrm{o}} & & \\ & \mathbb{D}_r^{\mathrm{o}} & \\ & & \mathbb{D}_r^{\mathrm{e}} \end{pmatrix}, \quad (n \text{ even}), \tag{B.8}$$

or

$$\mathbb{D}_r^{\otimes} = \begin{pmatrix} \mathbb{D}_r^{\mathrm{e}} & & \\ & \mathbb{D}_r^{\mathrm{e}} & \\ & & \mathbb{D}_r^{\mathrm{o}} \end{pmatrix}, \quad (n \text{ odd}). \tag{B.9}$$

For the periodic azimuthal grid

$$\theta_j = \frac{2\pi}{N} j, \quad j = 0, \ldots, N-1, \tag{B.10}$$

we use the standard periodic differentiation matrix

$$(\mathbb{D}_\theta)_{ij} = \begin{cases} \dfrac{(-1)^{i+j}}{2\sin\frac{(i-j)\pi}{N}}, & i \neq j \\ 0, & i = j \end{cases}, \tag{B.11}$$

where we assume that N is odd, see (Fornberg, 1996).

Finally, for the periodic axial grid

$$z_i = \frac{Q}{N} i, \quad i = 0, \ldots, N-1, \tag{B.12}$$

we make use of the differentiation matrix

$$(\mathbb{D}_z)_{ij} = \begin{cases} \dfrac{2\pi}{Q}\dfrac{(-1)^{i+j}}{2\sin\frac{(i-j)\pi}{N}}, & i \neq j \\ 0, & i = j \end{cases}. \tag{B.13}$$

References

G. K. Batchelor, 1967, *An Introduction to Fluid Dynamics.* Cambridge University Press.

L. Boberg and U. Brosa, 1988, Z. Naturforsch., A: Phys. Sci. **43**, 697-726.

J. P. Boyd, 1999, *Chebyshev and Fourier Spectral Methods.* Dover.

U. Brosa, 1989, *Turbulence without strange attractor*, J. Stat. Phys., **55**, 1303-1312.

C. Canuto, M.Y. Hussaini, A. Quarteroni, T.A. Zang, 1988, *Spectral Methods in Fluid Dynamics.* Springer-Verlag.

S. M. Cox and P. C. Matthews, 2001, *Exponential time differencing for stiff systems.* Submitted to J. Computational Physics.

A. G. Darbyshire & T. Mullin, 1995, *Transition to turbulence in constant-mass-flux pipe flow.* J. Fluid Mech. **289**, 83-114.

P. G. Drazin and W. H. Reid, 1981, *Hydrodynamic Stability.* Cambridge University Press.

B. Fornberg, 1996, *A Practical Guide for Pseudospectral Methods*, Cambridge University Press.

E. Hairer and G. Wanner, 1991, *Solving Ordinary Differential Equations II: Stiff and Differential-Algebraic Problems.* Springer-Verlag.

A. Iserles, 1996, *A First Course in the Numerical Analysis of Differential Equations*, Cambridge University Press.

J. Komminaho, 2000, *Direct Numerical Simulation of Turbulent Flow in Plane and Cylindrical Geometries.* Doctoral Thesis, Royal Institute of Technology, Stockholm.

M. T. Landahl, 1980, *A note on an algebraic instability of inviscid parallel shear flows*, J. Fluid Mech., **98**, 243-251.

A. Leonard and W. Reynolds, 1988, *Turbulent research by numerical simulation*, in *Perspectives in Fluid Mechanics*, D. Coles (Ed.), pp. 113-142, Springer-Verlag, New-York.

A. Leonard and A. Wray, 1982, *A new numerical method for the simulation of three dimensional flow in a pipe.* Proceedings, 8th Int. Conf. on Numerical Methods in Fluid Dynamics, E. Krause (Ed.), Springer-Verlag, Berlin.

A. Meseguer and L. N. Trefethen, 2000, *A spectral Petrov-Galerkin formulation for pipe flow I: Linear stability and transient growth.* Oxford University, Numerical Analysis Group, Report **00/18**.

P. L. O'Sullivan and K. S. Breuer, 1994, *Transient growth in circular pipe flow. II. Nonlinear development*, Phys. Fluids **6**(11), 3652-3664.

V. G. Priymak and T. Miyazaki, 1998, *Accurate Navier-Stokes Investigation of Transitional and Turbulent Flows in a Circular Pipe*, J. Comp. Phys. **142**, 370–411.

S. C. Reddy, P. J. Schmid, J. S. Baggett and D. S. Henningson, 1998, On stability of streamwise streaks and transition thresholds in plane channel flows. J. Fluid Mech., **365**, 269-303.

P. J. Schmid and D. S. Henningson, 1994, *Optimal energy growth in Hagen-Poiseuille flow.* J. Fluid Mech., **277**, 197-225.

P. J. Schmid and D. S. Henningson, 2001, *Stability and Transition in Shear Flows*, 2001, Springer-Verlag, New York.

H. Shan, B. Ma, Z. Zhang & F. T. M. Nieuwstadt, *Direct Numerical Simulation of a Puff and Slug in Transitional Cylindrical Pipe Flow*, 1999, J. Fluid Mech., **389**, 39-60.

L. N. Trefethen, 2000, *Spectral Methods in* Matlab, SIAM, Philadelphia.

D. J. Tritton, 1988, *Physical Fluid Dynamics*, Oxford University Press.

H. Yosida, 1990, *Construction of higher order symplectic integrators.* Phys. Lett. A **150**, pp. 262-268.

S. Wiggins, 1990, *Introduction to Applied Non-linear Dynamical Systems and Chaos*, Springer-Verlag, New York.

O. Y. Zikanov, 1996, *On the instability of pipe Poiseuille flow.* Phys. Fluids **8**(11), 2923-2932.